Oxygen Vacancies Evoked Blue TiO_2(B) Nanobelts with Efficiency Enhancement in Sodium Storage Behaviors

Yan Zhang, Zhiying Ding, Christopher W. Foster, Craig E. Banks, Xiaoqing Qiu, and Xiaobo Ji

Dr. Y. Zhang, Prof. Z. Ding, Prof. X. Qiu, Prof. X. Ji College of Chemistry and Chemical Engineering Central South University

Changsha 410083, China E-mail: xji@csu.edu.cn

Dr. C. W. Foster, Prof. C. E. Banks Faculty of Science and Engineering Manchester Metropolitan University Manchester M1 5GD, UK

Oxygen vacancies (OVs) dominate the physical and chemical properties of metal oxides, which play crucial roles in the various fields of applications. Density functional theory calculations show the introduction of OVs in TiO2(B) gives rise to better electrical conductivity and lower energy barrier of sodiation. Here, OVs evoked blue TiO2(B) (termed as B-TiO2(B)) nanobelts are successfully designed upon the basis of electronically coupled conductive polymers to TiO2, which is confirmed by electron paramagnetic resonance and X-ray photoelectron spectroscopy. The superiorities of OVs with the aid of carbon encapsulation lead to higher capacity (210.5 mAh g-1 (B-TiO2(B)) vs102.7 mAh g-1 (W-TiO2(B)) at 0.5 C) and remarkable long-term cyclability (the retention of 94.4% at a high rate of 10 C after 5000 times). In situ X-ray diff- ractometer analysis spectra also confirm that an enlarged interlayer spacing stimulated by OVs is beneficial to accommodate insertion and removal of sodium ions to accelerate storage kinetics and preserve its original crystal structure. The work highlights that injecting OVs into metal oxides along with carbon coating is an effective strategy for improving capacity and cyclability performances in other metal oxide based electrochemical energy systems.

1. Introduction

The physical and chemical properties of metal oxides, especially the color and electric features, are dominated by bulk defects such as oxygen vacancies (OVs) and consequently receive enor- mous attention in a myriad of applications, including catalyst, photocatalytic hydrogen evolution, and energy storage.[1] In sodium-ion batteries (SIBs), the existence of OVs may act as an electronic charge carrier to significantly enhance the electronic conductivity, which is beneficial to fast ion/electronic transport and enlarged sodium ion diffusion coefficients.[2] Surprisingly, the influences of OVs on rate capabilities and cycle perfor- mances in SIBs have been seldom investigated. In particular, the relevant work that the effect of OVs for bronze type TiO_2 (TiO_2(B)) on sodium energy storage is currently missing.

TiO_2(B), since the first preparation by Marchand et al. in 1980,[3] is less well known than rutile, anatase, or brookite. In fact, TiO_2(B) has a monoclinic structure with space group C2/m, which is con- structed by corrugated sheets of edge- and corner-sharing TiO_2 octahedral that are linked together by bridging oxygen atoms to form a 3D network. This cell structure results in a lower packing density, more open voids, and parallel channels in con- trast to other phases of TiO_2, and was considered as the best candidate for inter- calation.[4] Sodium ion intercalation was found to be highly feasible and more ener- getically preferred in TiO_2(B) compared with the type of rutile and anatase by Dawson and Robertson, although anatase was suggested as the best Li intercalation option.[5] Up to now, the sodium storage performances of TiO_2(B) were not greatly satisfied when considering its inefficient ion diffusion and poor electronic conductivity.[6] OVs can act as shallow donors, reducing the band gap (E_g) and raising the density of states (DOSs) below the Fermi level for TiO_2, which might afford helpful effects upon electronic structure.[7] It is expected that OVs incorporated into TiO_2(B) can effectively lead to the improvement of electronic conductivity, and also trigger remarkably the color from white to blue.[8] However, given that the function of OVs was weakened and interfered by decomposition of electrolyte and formation of solid–electrolyte interphase (SEI), which could be useful strategy to settle by surface covering.[2a] A surface coating on the electrode surface/active sites behaves as a mechanically stable kinetic barrier that protects electrolytes from directly contacting a bare electrode surface by suppressing undesirable side reactions between the electrode active sites and electrolytes, thus preventing excessive amounts of SEI formation.[9] Currently, recent work has proved that the Al_2O_3 coated on MoO_{3-x} surface by atomic layer deposition method played a protective role as an “artificial” SEI layer, which ensured the proper functioning of OVs on sodium energy storage of MoO_{3-x}.[2a] In fact, conductive carbon layer might be encouraged to be advantageous approach to insuring the effect of OVs; the formation of chemical bonds between carbon species and host materials can stabilize the OVs.[2a,10]

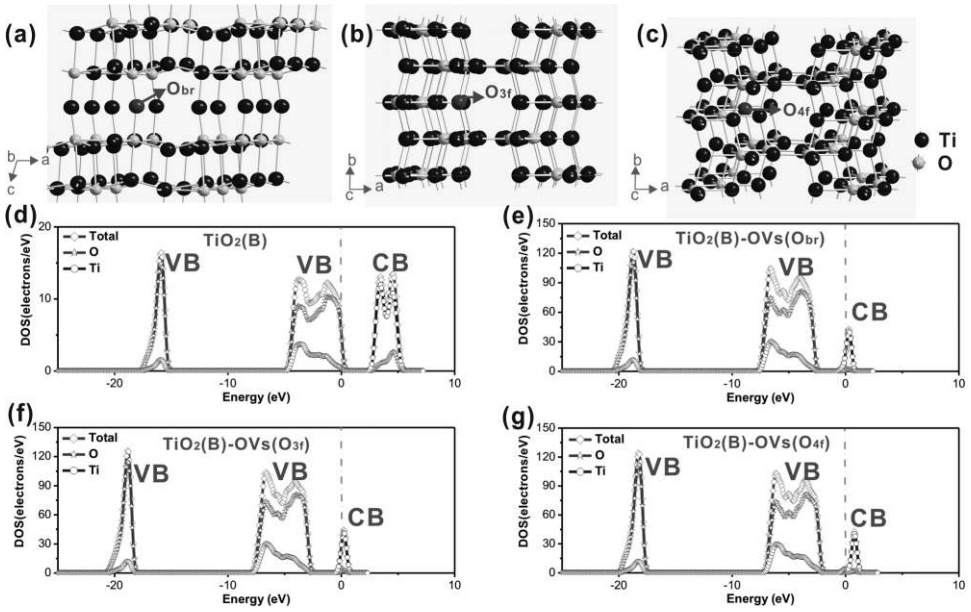

Figure 1. Three different sites for OVs: a) O_{br}, b) O_{3f}, c) O_{4f}; and calculated density of states (DOSs) and partial density states (PDOSs): d) TiO_2(B), e) TiO_2(B)-OVs(O_{br}), f) TiO_2(B)-OVs(O_{3f}), g) TiO_2(B)-OVs(O_{4f}).

Another interesting feature is that the presence of OVs can preserve crystal structure, and further can induce positive effects upon energy storage properties. For instance, OVs expanded the interlayer distance of ǀ ǀ-MoO_3 and enhanced pseudocapacitive charge storage properties, reported by Kim et al.[1d]

Herein, for the first time, the introduction of OVs evoking blue TiO_2(B) (termed as B-TiO_2(B)) accompanied with a carbon coating are simultaneously designed through the redox reaction of electronically coupled conductive polymers (CPs) at the TiO_2. Density functional theory (DFT) calculations shed light on regarding electronic properties, lattice interlayer spacing, OVs site, and the energy barrier of sodium intercalation. As proved by the in situ X-ray diffractometer (XRD) measurement, the expanded interlayer spacing and the lower energy barrier of sodiation arising from OVs is beneficial to preserve the integrity of the crystal structure and accelerate storage kinetics. Addition- ally, the combination of OVs and carbon wrapping result in an improved electric conductivity allowing fast electronic transports. These superiorities of OVs with the help of surface coating can promote favorable sodium ions insertion and efficiently enhance an enlarged sodium ion flux especially at high current densities, making B-TiO_2(B) nanobelts anode exhibits a remarkable high-rate and superior cyclability in comparison to those of TiO_2(B) without the existence of OVs and carbon species (termed as W-TiO_2(B)).

2. Results and Discussion

2.1. DFT Calculations Based on Oxygen Vacancies

As noted, in evaluating the influence of OVs upon the structural and energy storage properties of the TiO_2-B host material, it is vital to know the exact location of OVs, which is explored by utilizing the CASTEP plane-wave DFT code. In the structure of TiO_2-B, the oxygen atoms have three nonequivalent local environments, including the bonding to the bridging oxygen atom (termed as O_{br}, **Figure 1**a), threefold coordinated oxygen atom (termed as O_{3f}, Figure 1b) and fourfold coordinated oxygen atom (termed as O_{4f}, Figure 1c).[11] As shown by DFT calculations results, the formation of oxygen vacancies at the O_{br} (termed as TiO_2(B)-OVs(O_{br}); coordinates: 0.37, 0.74, 0.50) and O_{3f} (termed as TiO_2(B)-OVs(O_{3f}); coordinates: 0.36, 0.50, 0.65) sites is significantly more favorable than that from the O_{4f} site (termed as TiO_2(B)-OVs(O_{4f}); coordinates: 0.26, 0.50, 0.33). Furthermore the oxygen vacancy configuration at the O_{3f} site exhibits the lowest energy barriers, suggesting that a vacancy structure at the O_{3f} site is the most energetically stable. Additionally, after introducing OVs into different sites of TiO_2-B (Figure 1d–g and Figure S1 (Supporting Information)), the Fermi level is shifted to the conduction band (CB), and the band gap between the discrete valence band (VB) and the CB are narrowed, corresponding to an improved electron conductivity stimulated by OVs.

Considering sodium intercalation sites of TiO_2(B), three types (labeled A1, A2, and C sites) have been proposed, which are illustrated in Figure S2a.[5,12] The A1 are fivefold coordinated site along the *c*-axis (Figure S2c, Supporting Information), and the A2 site is also fivefold coordinated with oxygen atoms, locating at between the bridging oxygens (O_{br}) within the (001) plane (Figure S2d, Supporting Information). The C site, namely, the square planar site, at the middle of a distorted octahedral position (Figure S2b, Supporting Information), is thermodynamically and energetically favorable for the Na^{+} intercalated ions in the *b*-axis channel.[11,13] Here, the calculation of intercalation energies on the C cite of TiO_2(B) and TiO_2(B) with oxygen vacancies on O_{3f} (termed as TiO_2(B)-OVs(O_{3f})) is displayed using DFT methods (**Figure 2**). The energy change (termed as $\Delta E_{\text{sodiation}}$) before and after sodiation is obtained according to the following formula

$$E_{\text{sodiation}} = E_{\text{sodiated TiO}} - E_{\text{TiO}} - E_{\text{Na}}$$

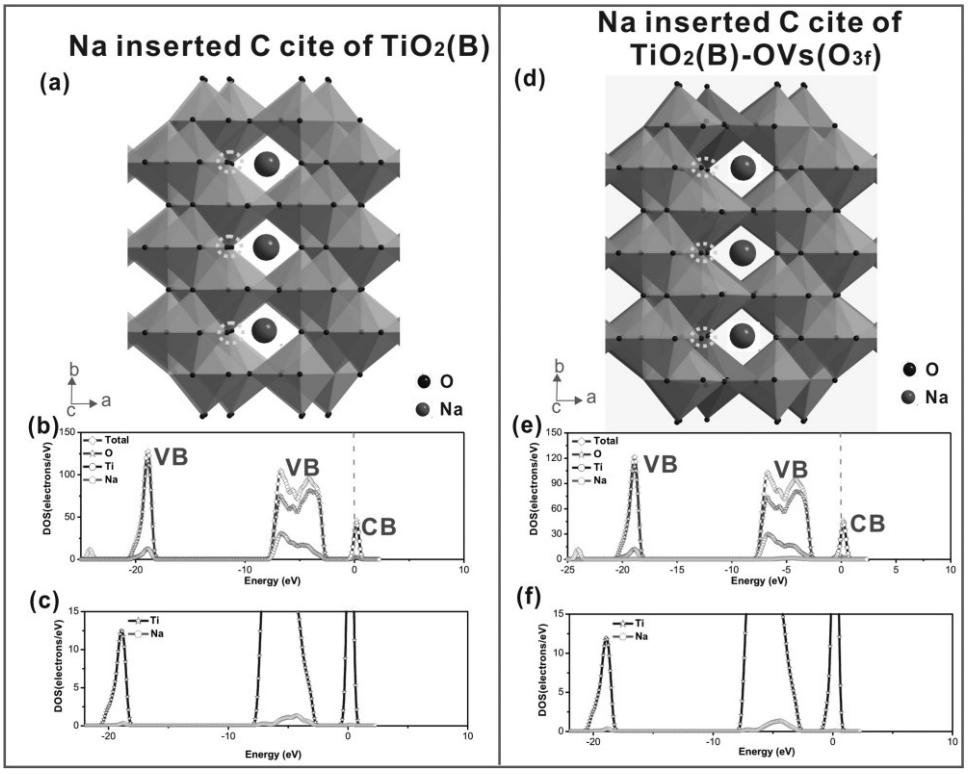

Figure 2. a) The structure models of Na-inserted TiO_2(B) and d) Na-inserted TiO_2(B)-OVs; the corresponding calculated density of states (DOSs) and partial density states (PDOSs): b,c) Na-inserted TiO_2(B), e,f) Na-inserted TiO_2(B)-OVs.

single layered titanates driven by the asymmetrical chemical environment and mechanical tensions tended to roll up and where $E_{\text{sodiated TiO}_2}$, E_{TiO2}, and E_{Na} represent the total energy of curve. The asymmetrical chemical environment arose from the Na-intercalated TiO_2(B), TiO_2(B), and Na ions, respectively, which are presented in Table S2 (Supporting Information). It has been computationally shown that TiO_2(B)-OVs(O_{3f}) possesses lower sodiated energy barriers, indicating that Na ion is more energetically favorable for insertion into TiO_2(B)-OVs compared with the pristine TiO_2(B) structure. Notably, in comparison with those of pristine TiO_2(B), despite of a smaller extent of movement of the CB and VB for sodiated TiO_2(B), the negative shifts of CB and VB are more noticeable (Figure 2 and Figure S1 (Supporting Information)), manifesting that OVs can enhance a higher activity toward sodium ions inserted/ extracted into/out TiO_2(B).

2.2. Material Characterization

As inspired by the positive influences of OVs on sodium ion intercalating in TiO_2(B), the OVs evoked blue TiO_2(B) nanobelts are successfully designed by redox reaction of pyrrole (Py) monomers. According to the preparation strategy of TiO_2 nanofibers/nanowires,[14] the formation pathway of TiO_2 nanobelts is proposed as illustrated in **Scheme 1**. In initial stages, under the existence of high concentrated NaOH solution, 1D TiO_2 particles were dissolved and epoxially grown into 2D layered nanosheets, which were further exfoliated into single layer structure and regarded as a stack of paper. Then, the imbalance of dangling bonds such as the negatively charged Ti||O|| and the positively charged Ti|| at the different edges of the nanosheets reacting with the hydroxide ions, leading to excessive surface energy.[14b,15] The mechanical tensions came from the imbalance in the layer width during spontaneous crystallization and rapid growth of layers, resulting in simulta- neous movement of the layer and scrolling of the nanosheet.[16] Note that both the diameter of the nanotubes and the struc- ture of nanobelts were determined by the kinetic rate of the nanosheets curving, the ratio of TiO_2(s) to $NaOH_{(aqueous)}$, hydro- thermal temperature, time, and especially stirring rate.[14d] Typically, the introduction of OVs was accomplished by the hydrogen and non-hydrogen routes,[17] including high-pres- sure hydrogenation[10b,18] and aluminum reduction.[10a] In our work, the incorporation of OVs was based on electronically coupled CPs to TiO_2, which simultaneously introduced the carbon coating. The polypyrrole (PPy) polymers with extending ||-conjugated electron systems, as conductive polymers, were direct oxidation of pyrrole (Py) monomers, which brought OVs into the crystal structure of TiO_2 accompanied with injecting electrons into the conduction band of TiO_2.[19]

The obtained white/blue-TiO_2(B) nanobelts are "cotton" like structure. Scanning electron microscopy (SEM) images of B-TiO_2(B) samples demonstrated the morphologies of intertwined belts with several micrometers length size (**Figure 3**a) and a coarse surface with small nanoparticles (Figure 3b,c). Although W-TiO_2(B) is also presenting ultralong interlinked nanobelts morpholo- gies (Figure S4a, Supporting Information), its surface is relatively smooth and clearly each nanobelt is consists of several continuous and parallel 1D structure (Figure S4b,c, Supporting Information). From the enlarged transmission electron micros- copy (TEM) images of W-TiO_2(B) (Figure S4d–f, Supporting Information), it shows that 1D structure is nanotubes with the widths of tens of nanometers size, which is confirmed by high-resolution TEM. For B-TiO_2(B) nanobelts, further characterized by TEM and HRTEM images, it is found that a few unique 1D nano- tubes with a highly oriented growth structure are constructed in every nanobelt (Figure 3e), suggesting that the oxidation treatment of pyrrole (Py) monomers cannot destroy nanotube structure embedded in nanobelts. Expectedly, enormous pores (diameters of 5–10 nm; Figure 3f,g) combined with some nanoparticles (size of 3–5 nm; Figure 3h) result in the island structure on the coarse surface of B-TiO_2(B) nanobelts. In particular, as seen from the HRTEM image (Figure 3i and Figure S4i (Supporting Information)), the d_{001}- and d_{110}- interlayer spacing of B-TiO_2(B) nanobelts are expanded to 0.65 nm and 0.37 nm, respectively, which can be attributed to the development of a wider van der Waals gap aroused by the OVs.[1d] The enlarger interplanar distance is beneficial to

accommodate sodium ion of large ionic radius insertion/extraction in B-TiO_2(B), leading to the long-term cycling stability.[20] Additionally, the HRTEM image (Figure 3h,i) and TEM elemental mapping of a single nanobelt (Figure 3g–j) can indicate that carbon species highly uniformly decorate B-TiO_2(B) nanobelts.

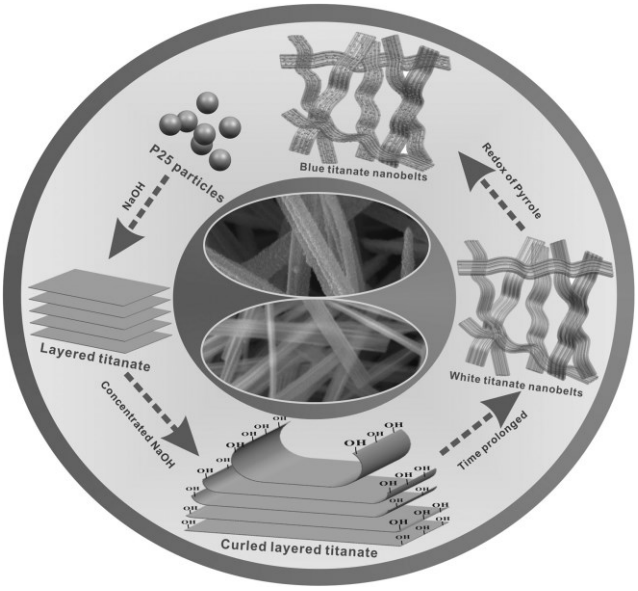

Scheme 1.

According to nitrogen adsorption–desorp- tion isotherm measurements, the W-TiO_2(B) nanobelts exhibit the distinct hysteresis loop at the relative pressure (P/P_0) range of 0.8–1.0, which can be identified as typical type IV curves (Figure S5a, Supporting Infor- mation). The hysteresis extended to P/P_0 1 manifests the unfilled large pores charac- teristic of the structures, corresponding to the pores between the nanotubes, which is well consistent with pore size distributions (Figure S5c, Supporting Information). For B-TiO_2(B) nanobelts, the hysteresis loop in the range of 0.45–1.0 P/P_0 is relatively broad, which is classified as a type-I isotherm with features of mesoporous structures inside aggregates of particles (Figure S5b, Sup- porting Information). Taking into account the morphology of the material shown by microscopy, the mesoporous may be ascribed to numerous pores in island structure and interparticle spaces in plentiful ultrasmall nanoparticles. Numerous pores (Figure S5c,d, Supporting Information) and interlinked structure provide a high specific surface area (B-TiO_2(B) nanobelts: 106.1 m^2 g^{-1}; W-TiO_2(B) nanobelts: 125.9 m^2 g^{-1}), which is expected to facilitate sufficient wetting with the Na-rich electrolyte.

As shown in **Figure 4**a, all synchrotron XRD patterns of the as-prepared two samples exhibit typical diffraction peaks of bronze phase (JCPDS 046-1238). For blue products, no additional phases such as anatase or rutile are observed, in spite of showing relatively weaker intensities and broader peaks in contrast to W-TiO_2(B) samples. What Kavan and co-workers[3,21] suggested is that phase-pure TiO_2(B) under alkaline hydro- thermal conditions was formed. However, the color of B-TiO_2(B) is visually translated from white to blue, which can commonly be attributed to the existence of OVs.[8b,10a,22] Raman scattering measurements are employed to explore the local structure properties of both the blue/white TiO_2(B) nanobelts. As shown in Figure 4b, the peak intensities of B-TiO_2(B) nanobelts turn to weaken too much compared with those of W-TiO_2(B) nanobelts, which could be attributed to the enhanced electronic conductivity of B-TiO_2(B) nanobelts. It is well known that good electronic conductivity can lower the skin depth of the incident photons with the reduction of Raman scattering intensities.[23] Additionally, even though the positions of all peaks are quite similar for two products, the slightly blue- shift of Raman peaks range from 100 to 900 cm^{-1} (Figure S6a, Supporting Information) and a much larger visible absorp- tion in UV region ranging from 400 to 800 nm^{-1} are noticed for B-TiO_2(B) nanobelts, proving the generation of a certain amount of OVs along with the color changes.[24] No other new band for W-TiO_2(B) nano- belts appears in more than 1000 cm^{-1} region, whereas the characteristic broad bands near 1347 and 1590 cm^{-1} are observed for B-TiO_2(B) nanobelts (Figure S6b, Supporting Information),

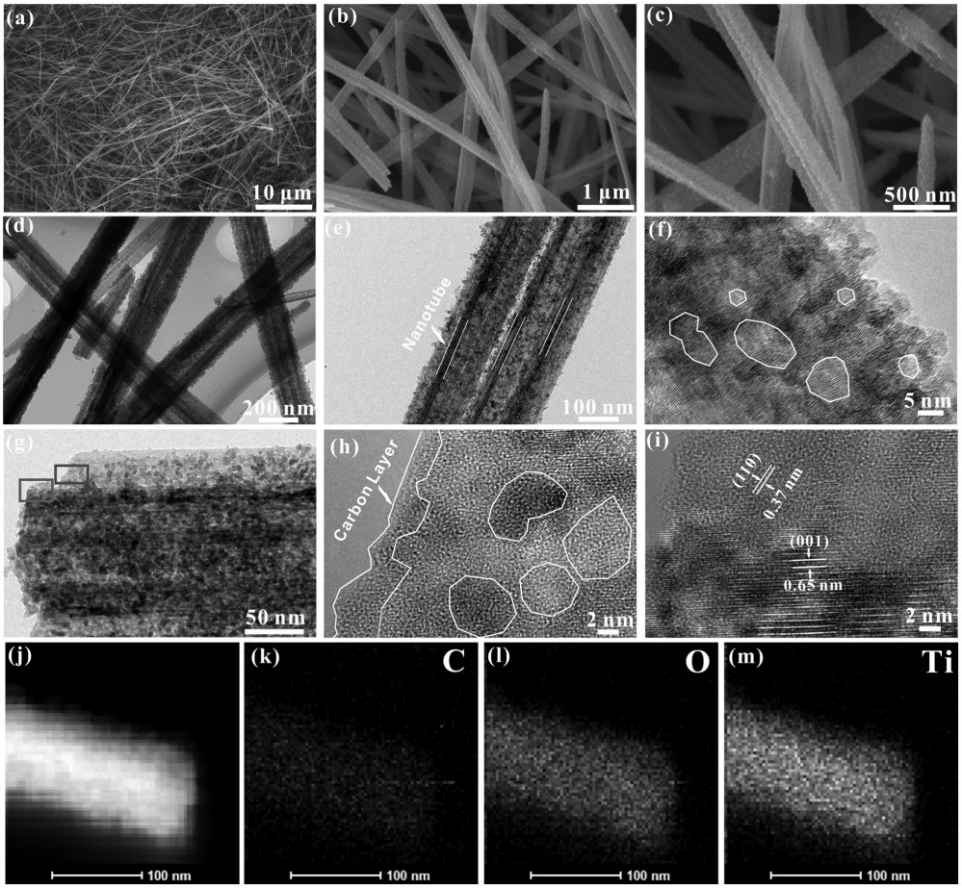

Figure 3. a–c) SEM images, d–g) TEM images, h,i) HRTEM images, j) the selected TEM image, and k–m) the corresponding EDX mapping images of B-TiO_2(B) nanobelts.

corresponding to carbon species.[25] Furthermore, it would be much convinced of the bronze phase purity of blue/white TiO_2(B) nanobelts, which is consistent with XRD analysis.

The existence of OVs is also illustrated by the X-ray photo- electron spectroscopy (XPS) spectra of C 1s, O 1s, and Ti 2p (Figure S7a, Supporting Information). The original C 1s XPS spectra in Figure S7b (Supporting Information) demonstrate that the peak at 283.59 eV is associated with C||Ti bond,[10d,24a,26] and others peaks at 284.82, 286.60, and 288.59 eV are assigned to C=C, C=O=C, and C=O bonds carbon species, respectively.[10c] The weight content of carbon for B-TiO_2(B) is only 2.5% in TG data (Figure S8, Supporting Information). Note that C=Ti bond would play an important role in the stabilization of the OVs centers in TiO_2 material.[10a] As shown in Figure 4c, after deconvolution, the Ti^{4+} species with Ti 2p3/2 and 2p1/2 signals at 458.63 and 464.35 eV for W-TiO_2(B) nanobelts are shifted to 458.54 and 464.26 eV for B-TiO_2(B) nanobelts, respectively. The bathochromic shifts phenomenon is as well corroborated by the peak of O 1s XPS spectra. These results confirm that the successful introduction of OVs and chemically bond between TiO_2(B) and carbon species.

Electron paramagnetic resonance (EPR) has been extensively employed to directly reveal the existence of the OVs as a result of the extremely sensitivity to detect paramagnetic species including unpaired electrons. As shown in Figure 4d, a significant EPR signal with a *g* value of 2.0007 is observed, which are well correlated with the OVs in the B-TiO_2(B) nanobelts.[24a,27] Notably, B-TiO_2(B) nanobelts exhibit a conductivity value of which is elevated by about five orders of magnitude in comparison with that of the W-TiO_2(B) nanobelts . The increase of electrical conductivity can be attributed to the combined effect of both the carbon coating and OVs.

2.3. Electrochemical Properties

To explore the influences of OVs with the help of carbon coating on sodium energy storage of TiO_2(B) electrode, two samples are assembled into the half-cells and investigated by typical cyclic voltammograms (CVs) at the scan rate of 0.1 mV s^{-1} between 0.01 and 3 V. As depicted by **Figure 5**a,b, in the initial cathodic sweep, the current response observed at 1.0–1.2 V is constantly stronger in contrast to the following four scans for two electrodes, which presumably is associated with the decomposition of electrolyte, the formation of SEI and irreversible trapping inside TiO_2(B). Two pairs of well-defined cathodic/anodic peaks emerged at 0.74/0.78 V (B-TiO_2(B)) and 0.68/0.80 V (W-TiO_2(B)) verify the reversible reduction/oxidative process

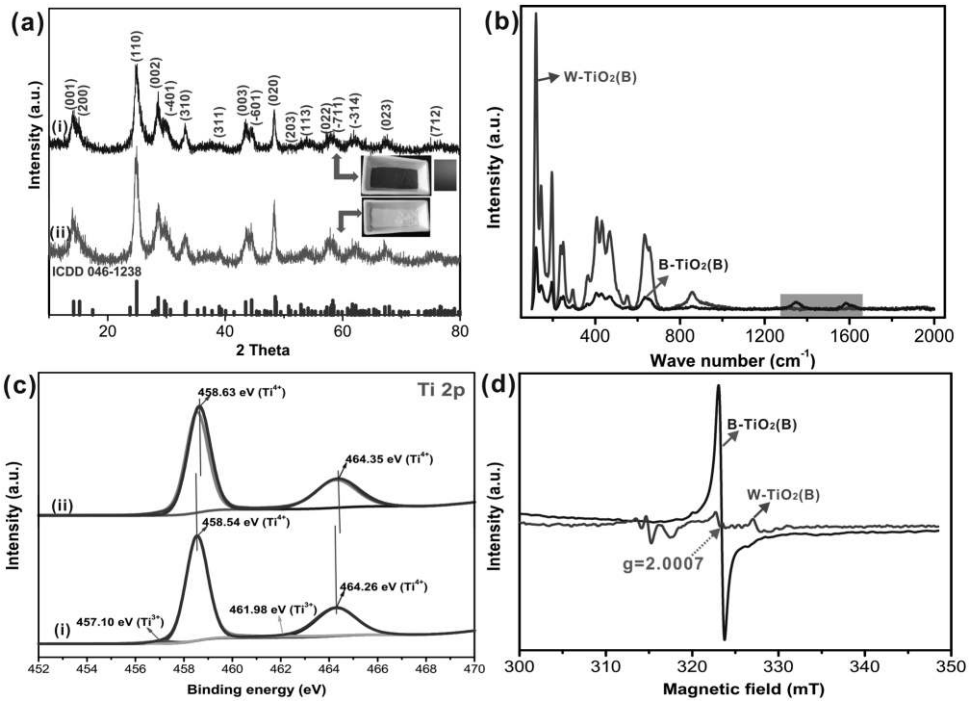

Figure 4. a) Synchrotron XRD spectra, b) Raman spectrum, c) Ti 2p XPS spectrum, and d) low-temperature EPR spectra of B-TiO_2(B) nanobelts (i) and W-TiO_2(B) nanobelts (ii).

between Ti^{4+} and Ti^{3+} (Figure 5a,b). Apparently, the lower deviation (the voltage deviation (ΔE) between the anodic and cathodic peaks) (B-TiO_2(B), 0.04 V; W-TiO_2(B), 0.12 V) between redox peaks and more pronounced peak intensity are observed in B-TiO_2(B) nanobelts electrode, suggesting the existence of OVs improved kinetics of TiO_2(B) anode.[1d,2a]

When cycled at 0.5 C rate (equal to 167.5 mA g^{-1}), the 1st, 2nd, 3rd, and 5th charge and discharge profiles for B-TiO_2(B) nanobelts (Figure S9a, Supporting Information) and W-TiO_2(B) nanobelts (Figure S9b, Supporting Information) are displayed, respectively. In the initial discharge curve, a slower trend of decrease in voltage at 1.1–1.5 V is presented, where the poten- tial drop turns to be rather sloped and no significant additional feature comes up in following cycles. As suggested by Passerini and co-workers,[6b] it is attributed to the formation of SEI and decomposition of the electrolyte. A sloped plateau like feature around 0.25–0.75 V in the discharge curve is derived from the reversible reactions of intercalation of sodium ions into bronze TiO_2. During the 1st to 5th charge process, a broad plateau appeared in the range of 0.6–1.2 V is always remained, corresponding to the reversible desodiation in TiO_2(B). The initial discharge capacity and charge capacity for W-TiO_2(B) nanobelts are 422.9 and 156.5 mAh g^{-1}, respectively. With respect to B-TiO_2(B) nanobelt, it displays a reversible discharge and charge capacities of 434.8 and 180.4 mAh g^{-1}, separately (Figure 5c). Apparently, B-TiO_2(B) nanobelts yielding the ini- tial Coulombic efficiency of 41.5% is higher than that of white TiO_2(B) nanobelts (37%) and is also superior to that of previously reported TiO_2 anodes in SIBs (Table S3, Supporting Information). The improved ini- tial Coulombic efficiency can be directly related to its enhanced

electronic conductivity, enlarged interlayer spacing and lower sodiated energy barriers stimulated by OVs, leading to more reversible trapping of sodium ion inside the TiO_2(B) lattice. Besides, carbon decorated on TiO_2(B) may protect electro- lytes from directly contacting a bare electrode surface, which may suppress undesirable side reactions and prevent exces- sive amounts of SEI formation, resulting in the efficiency enhancement of the reverse reaction at the first charge pro- cess.[28] After cycled 500 times, a high charge-specific capacity of 210.5 mAh g^{-1} is well maintained for B-TiO_2(B) nanobelts anode (Figure 5c). For W-TiO_2(B) electrode, the initial capacity value is 156.5 mAh g^{-1} at 0.5 C rate, and after 300 discharge– charge cycles, the specific capacity declines rapidly and finally remains 102.7 mAh g^{-1}. Notably, the obvious capacity loss is observed after 350 cycles, and the similar phenomenon also appears in different current densities. When the current density is higher, the sign of the capacity fading occurs ahead of time. This decay behavior may be attributed to the inferior adhesion strength between the active materials and carboxymethyl cellulose (CMC) binder along with a current rush and sodium ion insertion/extraction shock.[29] Clearly, during preliminary 8–23 cycles, for B-TiO_2(B)electrode, it displays a gradually increasing of capacity (the charge capacity from 170.5 to 188.7 mAh g^{-1}). Such a phenom- enon can be ascribed to an electrochemical activation process, which is similar to the case of anatase.[30] Meanwhile, the Cou- lombic efficiency of B-TiO_2(B) electrode after cycling 13 times ascends to 98.69% where the sodiation/desodiation process becomes almost revers- ible, while that of W-TiO_2(B) electrode reaches to 95.57% in the 20th cycle, which can be attributed to its low conductivity.

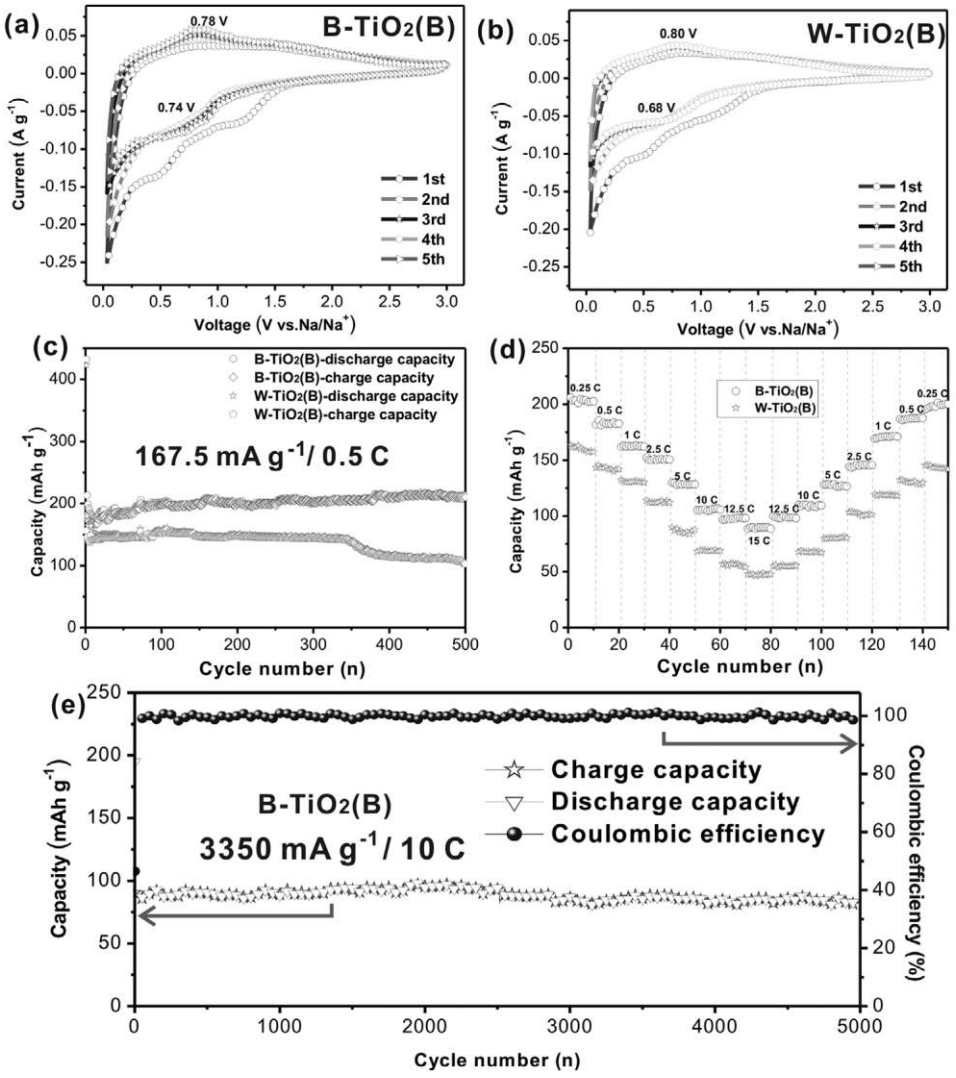

Figure 5. CV curves of a) blue TiO_2(B) nanobelts electrode and b) white TiO_2(B) nanobelts electrode at the scan rate of 0.1 mV s^{-1} in a voltage range of 0.01–3.0 V versus Na/Na^+. c) The cycling performances at 0.5 C (167.5 mA g^{-1}); d) rate performances; and e) long-term cycling performance at a rate of 10 C (3350 mA g^{-1}) for B-TiO_2(B) nanobelts electrode.

Comparatively speaking, better cycling stability and higher spe- cific capacity for B-TiO_2(B) electrode could be closely associated with the presence of OVs on the surface of the material during (de)sodiation process, which is evidenced by the characteristic EPR response with a g value of 2.0017 after ten cycles at 0.5 C rate as depicted in Figure S11 (Supporting Information).

Furthermore, the rate performances of two samples are evaluated (Figure 5d and Figure S12 (Supporting Information)). Along with the increase of the current density from 0.25 C to 12.5 C, for B-TiO_2(B) electrode, the charge specific capacity of 204.6, 182.5, 162.9, 150.9, 134.7, 114.9, and 106.8 mAh g^{-1} are delivered, separately. For comparison, the charge capacity values for W-TiO_2(B) electrode fade drastically from 160.3 (0.25 C) to 55.6 mAh g^{-1} (12.5 C). Notably, when charged/ discharged at high rates of 15 C, an ultrahigh charge specific capacity of 89.8 for B-TiO_2(B) electrode is more than double of that of W-TiO_2(B) electrode. This capacity is superior to that of pure bronze so far, and can also be comparable to that of

other reported representative TiO_2 works (**Table 1**), indicating the remarkable high-rate performances of B-TiO_2(B) electrode in SIB. Furthermore, when the galvanostatic rate recovers to be 12.5, 10, 5, 2.5, 1, 0.5, and 0.25 C, the reversible (charge) capacity of B-TiO_2(B) electrode is found to be 98.1, 108.4, 126.3, 145.5, 170.5, 186.4, and 200.3 mAh g^{-1}, respectively. It also indi- cates that the equivalent electrons and sodium ions are available simultaneously by the combination of OVs and carbon coating, leading to the efficiently improvement of the cyclability, even at high rates.[2a]

B-TiO_2(B) electrode, one most impressive feature, is cycled for 5000 times at a high rate of 10 C (equal to 3350 mA g^{-1}), still exhibiting a capacity of 80.9 mAh g^{-1} with the retention of 94.4% (with respect to the fifth cycle) (Figure 5e). In contrast to the sodium-storage capability of the bronze and anatase titania , the as-obtained B-TiO_2(B) nanobelts electrode here illuminates a marvelous endurable stability and extraordinary sustainability, revealing the effective and strong synergistic

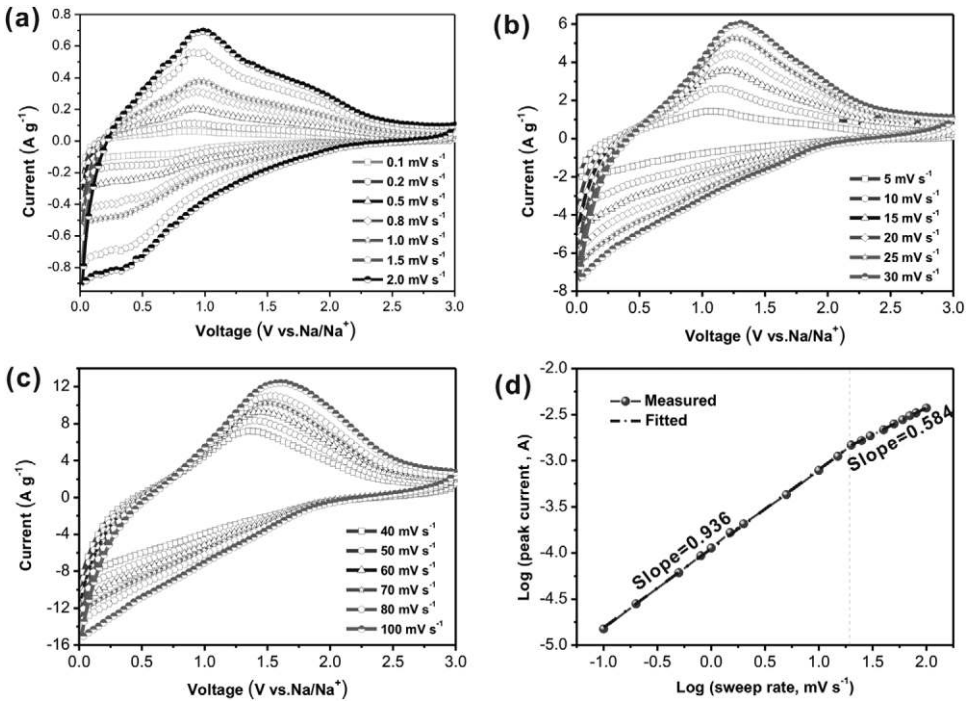

Figure 6. a–c) CV curves at various scan rates from 0.1 to 100 mV s^{-1} of B-TiO_2(B) nanobelts electrode and d) the relationships between the peak currents and scan rates in logarithmic format to determine the *b*-value for B-TiO_2(B) nanobelts electrode.

effect of OVs and carbon coating for enhancement of sodium storage of B-TiO_2(B) electrodes. Additionally, the Coulombic efficiency climbs to 99.2% after cycled 12 times and kept around 99% steadily in following cycles, further verifying the favorable reversibility of blue bronze sample.

To gain further insights into OVs and carbon wrapping impact on sodium storage behavior, CV tests of the fresh Na half-cell in different sweep rates range from 0.1 to 100 mV s^{-1} are explored for the electrochemical kinetics related to fara- daic redox processes (**Figure 6** and Figure S13 (Supporting Information)). Although CV curves of W-TiO_2(B) electrode at different scan rates (Figure S13a–c, Supporting Informa- tion) display the similar variation phenomenon, the inten- sities of peaks are weaker and electrode polarizations (ΔE: 0.12–0.69 V) are larger. For B-TiO_2(B) electrode, it is found that the shapes of peaks and deviation (ΔE: 0.04–0.59 V) between redox peaks still well reserved at various sweep rates from 0.1 to2.0 mV s^{-1} (Figure 6a and Figure S13a (), even when the sweep rates elevated from 5 to 100 mV s^{-1} (Figure 6b,c and Figure S13b,c (Supporting Information)), the characteristic of oxidative peak remains nearly identical. These results signify OVs combined with carbon coating can enhance the electrochemical kinetics of B-TiO_2(B) electrode, leading to more reversible sodium ion insertion or extraction. In general, two typical types, the faradaic behavior arising from sodium insertion and extraction mechanisms, and pseudocapacitive process owing to the surface faradic redox reactions, are recom- mended as deeply exploring electrode reaction mechanisms of sodium storage based on CV analysis at different sweep rates.[10c,30d,31] Both relationships are subsequently portrayed by plotting log(i) against log(v) for white/blue-TiO_2(B) electrode, where the *b*-values are obtained from the slopes. When the linear relationship (*b*-value of 1.0) existed between the peak cur- rent (i) and the scan rate (v), sodium storage is dominated by a pure capacitive behavior. However the current and the root square of sweep rates ($v^{1/2}$) is in proportion correlation (*b*-value of 0.5), corresponding to the faradaic mechanisms controlled by a total diffusion process. As the sweep rates heighten from 0.1 to 20 mV s^{-1},

the *b*-values of B-TiO_2(B) electrode approximately closes to 0.95 (Figure 6d), meaning that the sodium storage is mainly controlled by the kinetics features of pseudocapaci- tance, which is responsible for a fast sodiation/desodiation pro- cess and long-term cyclability. In contrast, the values of about 0.80 range from 0.1 to 10 mV s^{-1} are exhibited for W-TiO_2(B) anode, suggesting the dominant surface storage process (Figure S13d, Supporting Information). In short, the sweep voltammetry results indicate that the incorporation of OVs combining carbon coating enhance pseudocapacitive storage behavior and improve electrochemical kinetics, boosting rate capability, and specific capacity of B-TiO_2(B) electrode.

To gain greater insight into the reversible sodium storage mechanism in TiO_2(B)-OV, in situ XRD analysis are presented in **Figure 7** and Figure S14 (Supporting Information). In the typical initial discharge curve, the reflection (110) at about 25 (2ı ı) is slightly shifted to the lower angles because of the expansion of the lattice (Figure 7a,b), indicating the reaction is not conversion of TiO_2 to Ti metal, but is the electrochemical reduction of $Ti^{4ı ı/3ı ı}$.[6b,30a,32] During charging process, a con- traction of lattice results in the diffraction peaks recovered to original Bragg peak positions, corresponding to the reversible desodiation in the sodiated TiO_2(B)-OVs. These observations indicate that an enlarged interlayer spacing caused by OVs is in favor of the reversibly insertion/extraction of sodium ion into/ out of the host structure of TiO_2(B) and preserves the integrity

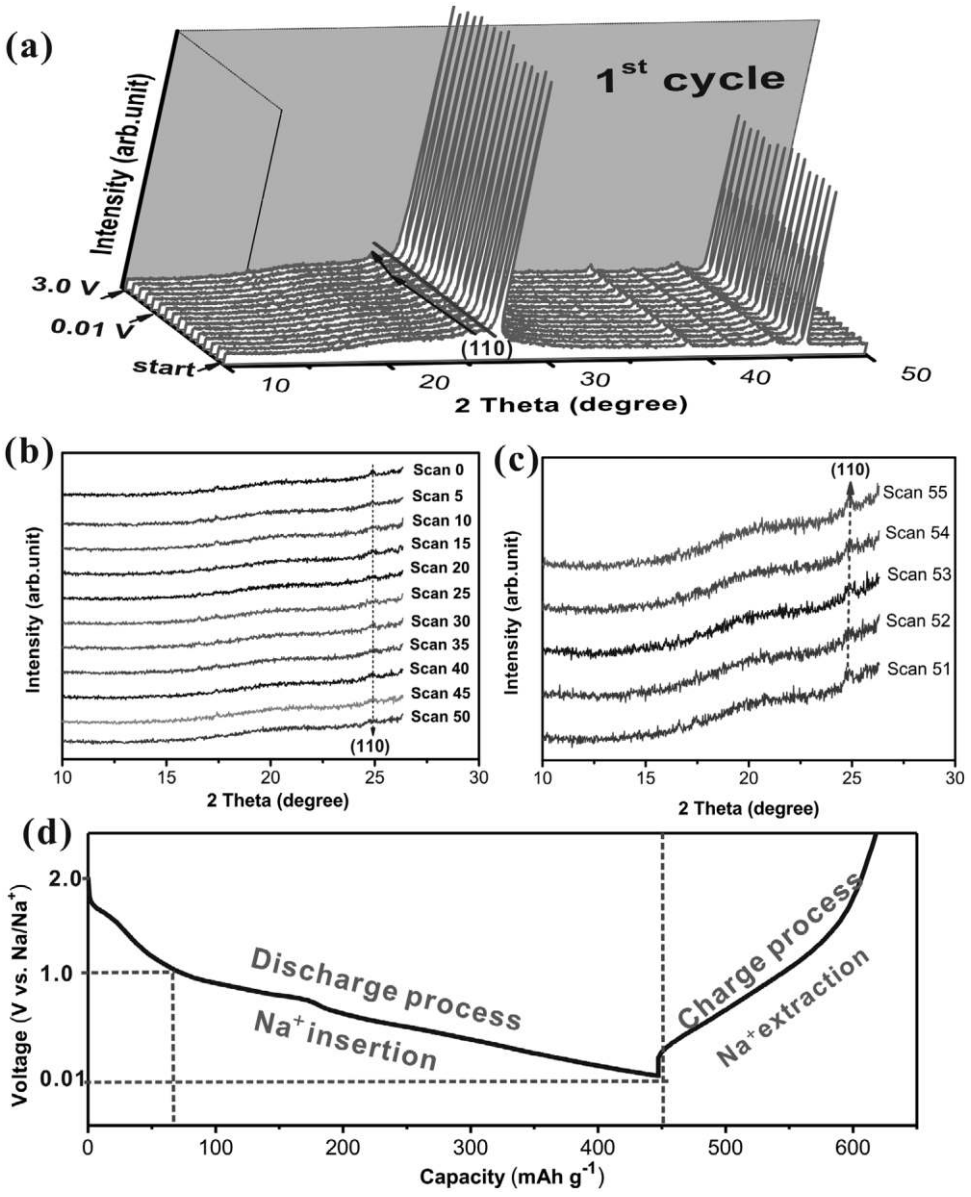

Figure 7. a) In situ XRD patterns of B-TiO_2(B) nanobelts anode during first cycle with a constant current of 87.5 mA g^{-1} (0.25 C-rate), b,c) the selected $2y$ region plot of the in situ XRD results at different discharge/charge states, and d) potential profile of the first (dis)charge cycle.

crystal the crystal structure during sodiation/desodiation pro- cess of TiO_2(B).

Herein, the creation of OVs via combination with carbon coating lead to B-TiO_2(B) nanobelts anode that presents a fast electrochemical kinetics and a superior sodium storage behavior including excellent high-rate performances and remarkably lengthened cyclability. It could be assigned to the following influence of OVs with the aid of carbon coating on the structural and chemical characteristic. Structurally, one vital impact of OVs causes the larger d_{001}- spacing (0.65 nm) and d_{110}- spacing (0.37 nm), leading to be indispensable for accom- modating larger sodium ions. Apparently, the expanded lattice galleries also can suppress sodium ion insertion induced the crystal transformation, ensuring in structure stability explain

why B-TiO_2(B) nanobelts exhibits more stable cycling perfor- mance. Furthermore, through the combination of OVs and carbon encapsulation, the electric conductivity of B-TiO_2(B) nanobelts increases approximately five orders of magnitude compared with that of W-TiO_2(B) nanobelts. The high electric conductivity can boost significantly transfer for electron, pro- moting an amplified sodium ion flux especially at high current densities. Total energy calculations also verify a lower energy barrier of TiO_2(B)-OVs(O_{3f}), resulting in more favorable sodium ions insertion into bronze structure. Notably, via jointing with the carbon coating, above the proper benefits of OVs are well accomplished, synergistically functioned for improved specific capacities, high-rate capabilities, and marvelous long-term cyclability of B-TiO_2(B) electrode.

3. Conclusion

In summary, blue-colored TiO_2(B) nanobelts derived from the introducing of OVs are successfully prepared on the basis of electronically coupled conductive polymers to TiO_2. It is dem- onstrated that B-TiO_2(B) possesses the morphologies of inter- twined nanobelts with several tens of micrometers length size, and nanobelts consist of ultralong nanotubes with an average widths of tens nanometers. Moreover, the precise location of OVs and the energy barrier of sodiated TiO_2(B)-OVs are first proposed based on CASTEP plane-wave DFT code. Together with its bulk structure, the introduction of OVs, and well-tailored chemically bonded interfaces, B-TiO_2(B) nanobelts exhibit the increased electronic conductivity, a lower sodiated energy barriers and fast electron/ion transfer, which is ben- eficial to accelerate Na^{+} adsorption and diffusion kinetics. Thereby, B-TiO_2(B) electrodes display the significantly supe- rior sodium-storage properties, including a higher capacity (0.5 C; 210.5 mAh g^{-1} vs 102.7 mAh g^{-1}), better rate perfor- mance (15 C; 89.8 vs 36.7 mAh g^{-1}), compared to those of pristine W-TiO_2(B) electrodes. Notably, even at the high rate of 10 C, the reversible capacity up to 5000 cycles can still maintain at 80.9 mAh g^{-1}. Such improvements could suggest an effective strategy to realize the optimal functions of OVs with the help of surface coating for electrochemical energy storage devices.

4. Experimental Section

Materials and Chemicals: All chemical reagents in our experiments, including titania P25 (TiO_2), sodium hydroxide (NaOH, pellets, anhydrous, 98%), nitric acid (HNO_3, 65%, Merck), hydrochloric acid (HCl, 37.5%, Merck), cetyltrimethyl ammonium bromide ($(C_{16}H_{33})N(CH_3)_3Br$ (CTAB), Merck), ammonium peroxydisulfate $(NH_4)_2S_2O_8$ (APS), Merck), pyrrole (C_4H_5N, 98%), were purchased from Sinopharm and used without any further treatment. Sodium metal foil (Na, 99%), super P (C, 35–45 nm in grain sizes), polyethylene film (Celgard 2500), CMC (≥ 99.5%), and propylene carbonate (PC, $C_4H_6O_3$, 99.7%) were purchased from Sigma-Aldrich. Sodium perchlorate ($NaClO_4$, ≥99%) and fluoroethylene carbonate (FEC, $C_3H_3FO_3$, ≥ 99%) additive were purchased from Alfa Aesar

Calculation Methods: All calculations were carried out employing the CASTEP plane-wave DFT code, on the basis of generalized gradient approximation of Perdew and Wang.[33] For total energy calculations, it used a plane-wave basis with a kinetic energy cutoff of 500 eV to ensured good convergence.

Material Preparation: In a typical procedure for white TiO_2 nanobelts, sodium hydroxide (18 g, 11.25 m) was fully dissolved in 40 mL deionized water, followed by adding the commercial titania P25 (0.3 g) precursor to form the homogenous milk solutions under intensively magnetic stirring. The as-prepared milky suspension was transferred into a Teflon-lined stainless steel autoclave (50 mL, capacity), and hydrothermally treated in a silicon oil bath for 48 h under 160 °C at the stirring rates of 500 rpm. After hydrothermal reaction, the autoclave was taken out from oil bath and cooled to room temperature. The as-prepared white flocculent products were centrifuged and washed with deionized water to reach a pH value of 9. Furthermore, the wet flocculent precipitations were ion exchange for five times in a diluted HNO_3 solution (0.1 m) to yield hydrogen titanate samples, and then again separated by centrifugation, washed extensively with deionized water to attain a neutral solution.

After drying at 100 oC for 12 h under vacuum, white TiO_2 precursor were annealed at 500 ı C for 2 h at the ramping rate of 3 oC min^{-1} in air to obtain W-TiO_2(B) nanobelts. In the preparation of B-TiO_2(B) nanobelts, 0.15 g CTAB was dissolved into 40 mL 0.1 m HCl under ice bath. After strongly stirring for 15 min, 200 mg W-TiO_2(B) precursor and 0.26 g APS were added into the as-prepared solution, and stirring constantly for 15 min. Then, pyrrole was dropped into above mixture reactive solution, and all solutions kept stirring at 0–5 ıC for 24 h all the time. The resulting blue flocculent of TiO_2 precursors were yield by centrifugation and washed with deionized water. Subsequently, after drying under vacuum, B-TiO_2(B) precursor were annealed at 500 C for 2 h at the ramping rate of 3 ıC min^{-1} under pure argon flow to protect OVs.

Material Characterization: The morphologies and structure of as-obtained products were analyzed by field emission scanning electron microscopy (FEI Quanta 200, Japan), TEM (FEI TecnaiG2F20, American), and HRTEM (JEOL JEM-2100F, Japan). The characteristics of elemental distribution were obtained via energy-dispersive X-ray spectroscopy (EDX, JEOL JEM-2100F, Japan). The crystal phase of products were determined by using an XRD (Rigaku D/max 2550 VB 18kW, Japan) (2 ı: 10 – 80 ; Cu K ı radiation; receiving slit, 0.1542 nm; scintillation counter, 40 mA; 40 kV) and a Laser Micro-Raman Spectrometer (Raman, Renishaw InVia, UK). The presence of OVs were examined by UV–vis diffuse reflectance spectroscopy (UV–vis, Shimadzu UV 3600, Japan), XPS (K-Alpha 1063, UK), and EPR (Bruker EMX-10/12, Germany), respectively. The conductivities were measured by the standard four- probe method at room temperature. The Brunauer–Emmett–Teller (Micrometrics ASAP2000, 77K, USA) specific surface areas and pores distributions were calculated on the basis of N_2 adsorption analysis.

Electrochemical Tests: A preparation of slurry was through admixing with carboxymethyl cellulose of 15% as binder and super P additive of 15% as conducting agent, a certain amount of water as solvent, and B-TiO_2(B) nanobelts or W-TiO_2(B) nanobelts powder of 70 wt% as active materials. And the anode pieces were obtained by undergoing the process of slurry printing, drying, and cutting. The mass loading of blue TiO_2(B) nanobelts electrode and white TiO_2(B) nanobelts electrode were tried to keep the same amount of 0.8–0.9 mg per square cm. CR2016-type coin cells, pure sodium metal foil as the counter and reference electrode, Celgard 2500 microporous film as the separator, a solution of 1 m $NaClO_4$ dissolving in a 95:5 (V/V) mixture of PC and FEC additive as the nonaqueous electrolyte were assembled in in a glove box (mBraun, Germany) filled with highly pure argon gas (O_2 and H_2O levels <0.5 ppm). The evaluation of sodium storage performances for half-cells was conducted on Solartron Analytical (Ametek; cyclic voltammetry, electrochemical impedance spectroscopy), Arbin battery cycler (BT2000; galvanostatic charge/discharge cycling and rate performance tests).

Acknowledgements

This work was financially supported by the National Natural Science Foundation of China (51622406, 21673298, and 21473258), the Innovation Mover Program of the Central South University (2016CX020), the Distinguished Young Scientists of the Hunan Province (13JJ1004), and the Fundamental Research Funds for the Central Universities of the Central South University (2016zzts022).

[1] a) Y. Sun, S. Gao, F. Lei, Y. Xie, *Chem. Soc. Rev.* **2015**, *44*, 623; b) Z. Luo, R. Miao, T. D. Huan, I. M. Mosa, A. S. Poyraz, W. Zhong, J. E. Cloud, D. A. Kriz, S. Thanneeru, J. He, *Adv. Energy Mater.* **2016**, *6*, 1600528; c) X. Chen, L. Liu, P. Y. Yu, S. S. Mao, *Science* **2011**, *331*, 746; d) H.-S. Kim, J. B. Cook, H. Lin, J. S. Ko, S. H. Tolbert, V. Ozolins, B. Dunn, *Nat. Mater.* **2017**, *16*, 454; e) J.-Y. Shin, J. H. Joo, D. Samuelis, J. Maier, *Chem. Mater.* **2012**, *24*, 543.

[2] a) Y. Xu, M. Zhou, X. Wang, C. Wang, L. Liang, F. Grote, M. Wu, Y. Mi, Y. Lei, *Angew. Chem. Int. Ed.* **2015**, *54*, 8768; b) X. Lu, G. Wang, T. Zhai, M. Yu, J. Gan, Y. Tong, Y. Li, *Nano Lett.* **2012**, *12*, 1690; c) Y. G. Guo, Y. S. Hu, W. Sigle, J. Maier, *Adv. Mater.* **2007**, *19*, 2087; d) P. Simon, Y. Gogotsi, B. Dunn, *Science* **2014**, *343*, 1210.

[3] R. Marchand, L. Brohan, M. Tournoux, *Mater. Res. Bull.* **1980**, *15*, 1129.

[4] a) A. S. Dalton, A. A. Belak, A. Van der Ven, *Chem. Mater.* **2012**, *24*, 1568; b) X. Hua, Z. Liu, P. G. Bruce, C. P. Grey, *J. Am. Chem. Soc* **2015**, *137*, 13612; c) H. Hu, L. Yu, X. Gao, Z. Lin, X. W. D. Lou, *Energy Environ. Sci.* **2015**, *8*, 1480; d) A. R. Armstrong, G. Armstrong, J. Canales, R. García, P. G. Bruce, *Adv. Mater.* **2005**, *17*, 862.

[5] J. A. Dawson, J. Robertson, *J. Phys. Chem. C* **2016**, *120*, 22910.

[6] a) J. Huang, D. Yuan, H. Zhang, Y. Cao, G. Li, H. Yang, X. Gao, *RSC Adv.* **2013**, *3*, 12593; b) L. Wu, D. Bresser, D. Buchholz, S. Passerini, *J. Electrochem. Soc.* **2015**, *162*, A3052.

[7] a) X. Lu, A. Chen, Y. Luo, P. Lu, Y. Dai, E. Enriquez, P. Dowden, H. Xu, P. G. Kotula, A. K. Azad, D. A. Yarotski, R. P. Prasankumar, A. J. Taylor, J. D. Thompson, Q. Jia, *Nano Lett.* **2016**, *16*, 5751; b) B. Sun, T. Shi, X. Tan, Z. Liu, Y. Wu, G. Liao, *J. Nanosci. Nano- technol.* **2016**, *16*, 6148.

[8] a) M. Li, W. Hebenstreit, U. Diebold, A. M. Tyryshkin, M. K. Bowman, G. G. Dunham, M. A. Henderson, *J. Phys. Chem. B* **2000**, *104*, 4944; b) J. Zheng, Y. Liu, G. Ji, P. Zhang, X. Cao, B. Wang, C. Zhang, X. Zhou, Y. Zhu, D. Shi, *ACS Appl. Mater. Inter- faces* **2015**, *7*, 23431.

[9] a) X. Meng, X.-Q. Yang, X. Sun, *Adv. Mater.* **2012**, *24*, 3589; b) X. Han, Y. Liu, Z. Jia, Y.-C. Chen, J. Wan, N. Weadock, K. J. Gaskell, T. Li, L. Hu, *Nano Lett.* **2014**, *14*, 139.

[10] a) J. Zheng, G. Ji, P. Zhang, X. Cao, B. Wang, L. Yu, Z. J. Xu, *Chem. - Eur. J.* **2016**, *22*, 7316; b) J. Zheng, L. Liu, G. B. Ji, Q. F. Yang, L. R. Zheng, J. Zhang, *ACS Appl. Mater. Interfaces* **2016**, *8*, 20075; c) C. Chen, Y. Wen, X. Hu, X. Ji, M. Yan, L. Mai, P. Hu, B. Shan, Y. Huang, *Nat. Commun.* **2015**, *6*, 6929; d) J. Chen, G. Zou, H. Hou, Y. Zhang, Z. Huang, X. Ji, *J. Mater. Chem. A* **2016**, *4*, 12591.

[11] C. Arrouvel, S. C. Parker, M. S. Islam, *Chem. Mater.* **2009**, *21*, 4778.

[12] L. Brohan, *Solid State Ionics* **1983**, *9*, 419.

[13] F. Legrain, O. Malyi, S. Manzhos, *J. Power Sources* **2015**, *278*, 197.

[14] a) Y.-F. Chen, C.-Y. Lee, M.-Y. Yeng, H.-T. Chiu, *Mater. Chem. Phys.* **2003**, *81*, 39; b) M. Leng, Y. Chen, J. Xue, *Nanoscale* **2014**, *6*, 8531; c) Y. Tang, Y. Zhang, J. Deng, D. Qi, W. R. Leow, J. Wei, S. Yin, Z Dong, R. Yazami, Z. Chen, *Angew. Chem.* **2014**, *126*, 13706; d) D. V. Bavykin, J. M. Friedrich, F. C. Walsh, *Adv. Mater.* **2006**, *18*, 2807.

[15] S. Zhang, L.-M. Peng, Q. Chen, G. Du, G. Dawson, W. Zhou, *Phys. Rev. Lett.* **2003**, *91*, 256103.

[16] D. V. Bavykin, V. N. Parmon, A. A. Lapkin, F. C. Walsh, *J. Mater. Chem.* **2004**, *14*, 3370.

[17] a) Z. Wang, C. Yang, T. Lin, H. Yin, P. Chen, D. Wan, F. Xu, F. Huang, J. Lin, X. Xie, *Adv. Funct. Mater.* **2013**, *23*, 5444; b) Z. Wang, C. Yang, T. Lin, H. Yin, P. Chen, D. Wan, F. Xu, F. Huang, J. Lin, X. Xie, *Energy Environ. Sci.* **2013**, *6*, 3007; c) T. Lin, C. Yang, Z. Wang, H. Yin, X. Lü, F. Huang, J. Lin, X. Xie, M. Jiang, *Energy Environ. Sci.* **2014**, *7*, 967.
[18] X. Chen, L. Liu, Y. Y. Peter, S. S. Mao, *Science* **2011**, *331*, 746.
[19] a) Q. Z. Luo, L. L. Bao, D. S. Wang, X. Y. Li, J. An, *J. Phys. Chem. C* **2012**, *116*, 25806; b) H.-C. Liang, X.-Z. Li, *Appl. Catal., B* **2009**, *86*, 8; c) N. M. Dimitrijevic, S. Tepavcevic, Y. Z. Liu, T. Rajh, S. C. Silver, D. M. Tiede, *J. Phys. Chem. C* **2013**, *117*, 15540; d) Z. Weng, X. Y. Ni, *J. Appl. Polym. Sci.* **2008**, *110*, 109; e) P. M. Dziewoński, M. Grzeszczuk, *Electrochim. Acta* **2010**, *55*, 3336.
[20] a) G. Longoni, R. L. Pena Cabrera, S. Polizzi, M. D'Arienzo, C. M. Mari, Y. Cui, R. Ruffo, *Nano Lett.* **2017**, *17*, 992; b) W. Luo, Z. Jian, Z. Xing, W. Wang, C. Bommier, M. M. Lerner, X. Ji, *ACS Cent. Sci.* **2015**, *1*, 516; c) Y. Cao, L. Xiao, M. L. Sushko, W. Wang, B. Schwenzer, J. Xiao, Z. Nie, L. V. Saraf, Z. Yang, J. Liu, *Nano Lett.* **2012**, *12*, 3783.
[21] M. Zukalova, M. Kalbac, L. Kavan, I. Exnar, M. Graetzel, *Chem. Mater.* **2005**, *17*, 1248.
[22] J. X. Qiu, S. Li, E. Gray, H. W. Liu, Q. F. Gu, C. H. Sun, C. Lai, H. J. Zhao, S. Q. Zhang, *J. Phys. Chem. C* **2014**, *118*, 8824.
[23] M. B. Yahia, F. Lemoigno, T. Beuvier, J.-S. Filhol, M. Richard-Plouet, L. Brohan, M.-L. Doublet, *J. Chem. Phys.* **2009**, *130*, 204501.
[24] a) V. Etacheri, J. E. Yourey, B. M. Bartlett, *ACS Nano* **2014**, *8*, 1491; b) C. Kim, S. Kim, S. P. Hong, J. Lee, J. Yoon, *Phys. Chem. Chem. Phys.* **2016**, *18*, 14370; c) Y. Zhang, Z. Xing, X. Liu, Z. Li, X. Wu, J. Jiang, M. Li, Q. Zhu, W. Zhou, *ACS Appl. Mater. Interfaces* **2016**, *8*, 26851.
[25] a) P. Dhanasekaran, S. V. Selvaganesh, S. D. Bhat, *J. Power Sources* **2016**, *304*, 360; b) W. Luo, Y. Wang, L. Wang, W. Jiang, S.-L. Chou, S. X. Dou, H. K. Liu, J. Yang, *ACS Nano* **2016**, *10*, 10524.
[26] J. H. Park, S. Kim, A. J. Bard, *Nano Lett.* **2006**, *6*, 24.
[27] M. Xing, J. Zhang, F. Chen, B. Tian, *Chem. Commun.* **2011**, *47*, 4947.
[28] a) W. M. Zhang, X. L. Wu, J. S. Hu, Y. G. Guo, L. J. Wan, *Adv. Funct. Mater.* **2008**, *18*, 3941; b) Y. Lai, W. Liu, J. Li, K. Zhang, F. Qin, M. Wang, J. Fang, *J. Alloys Compd.* **2016**, *666*, 254.
[29] a) W.-J. Li, S.-L. Chou, J.-Z. Wang, H.-K. Liu, S.-X. Dou, *Chem. Commun.* **2015**, *51*, 4720; b) C. Zhu, K. Song, P. A. van Aken, J. Maier, Y. Yu, *Nano Lett.* **2014**, *14*, 2175; c) H. Zhao, Z. Wang, P. Lu, M. Jiang, F. Shi, X. Song, Z. Zheng, X. Zhou, Y. Fu, G. Abdelbast, X. Xiao, Z. Liu, V. S. Battaglia, K. Zaghib, G. Liu, *Nano Lett.* **2014**, *14*, 6704; d) S.-L. Chou, X.-W. Gao, J.-Z. Wang, D. Wexler, Z.-X. Wang, L.-Q. Chen, H.-K. Liu, *Dalton Trans.* **2011**, *40*, 12801.
[30] a) L. Wu, D. Bresser, D. Buchholz, G. A. Giffin, C. R. Castro, A. Ochel, S. Passerini, *Adv. Energy Mater.* **2015**, *5*, 1401142; b) Y. Zhang, Y. Yang, H. Hou, X. Yang, J. Chen, M. Jing, X. Jia, X. Ji, *J. Mater. Chem. A* **2015**, *3*, 18944; c) Y. Zhang, C. Wang, H. Hou, G. Zou, X. Ji, *Adv. Energy Mater.* **2017**, *7*, 1600173; d) M. Zhou, Y. Xu, J. Xiang, C. Wang, L. Liang, L. Wen, Y. Fang, Y. Mi, Y. Lei, *Adv. Energy Mater.* **2016**, *6*, 1600448.
[31] a) Y. Zhu, L. Peng, D. Chen, G. Yu, *Nano Lett.* **2015**, *16*, 742; b) X. Deng, K. Xie, L. Li, W. Zhou, J. Sunarso, Z. Shao, *Carbon* **2016**, *107*, 67; c) Y. Zhang, C. W. Foster, C. E. Banks, L. Shao, H. Hou, G. Zou, J. Chen, Z. Huang, X. Ji, *Adv. Mater.* **2016**, *28*, 9391.

[32] a) J.-Y. Hwang, S.-T. Myung, J.-H. Lee, A. Abouimrane, I. Belharouak, Y.-K. Sun, *Nano Energy* **2015**, *16*, 218; b) K.-T. Kim, G. Ali, K. Y. Chung, C. S. Yoon, H. Yashiro, Y.-K. Sun, J. Lu, K. Amine, S.-T. Myung, *Nano Lett.* **2014**, *14*, 416.
[33] J. P. Perdew, Y. Wang, *Phys. Rev. B* **1992**, *46*, 12947.
[34] Y. Xu, M. Zhou, L. Wen, C. Wang, H. Zhao, Y. Mi, L. Liang, Q. Fu, M. Wu, Y. Lei, *Chem. Mater.* **2015**, *27*, 4274.
[35] J. Ni, S. Fu, C. Wu, J. Maier, Y. Yu, L. Li, *Adv. Mater.* **2016**, *28*, 2259.
[36] M. Zhou, Y. Xu, C. Wang, Q. Li, J. Xiang, L. Liang, M. Wu, H. Zhao, Y. Lei, *Nano Energy* **2017**, *31*, 514.